MATERIALS CHARACTERIZATION 94 (2014) 126–137

Available online at www.sciencedirect.com

ScienceDirect

www.elsevier.com/locate/matchar

Powder metallurgy processing and deformation characteristics of bulk multimodal nickel

L. Farbaniec[a,1], G. Dirras[a,*], A. Krawczynska[b], F. Mompiou[b], H. Couque[c], F. Naimi[d], F. Bernard[d], D. Tingaud[a]

[a]Université Paris 13, Sorbonne Paris Cité, LSPM, CNRS, 99 Avenue J.B. Clément, 93430 Villetaneuse, France
[b]Université Paul Sabatier, CEMES, CNRS, 29 rue Jeanne Marvig 31055 Toulouse, France
[c]Nexter Munitions, 7 route de Guerry, 18200 Bourges, France
[d]Institut Carnot de Bourgogne, UMR 6303 CNRS, Université de Bourgogne, BP 47870, 21078 Dijon, France

ARTICLE DATA

Article history:
Received 11 February 2014
Received in revised form 3 May 2014
Accepted 8 May 2014
Available online 22 May 2014

Keywords:
Multimodal nickel
Spark plasma sintering
EBSD
In-situ TEM
Plasticity

ABSTRACT

Spark plasma sintering was used to process bulk nickel samples from a blend of three powder types. The resulting multimodal microstructure was made of coarse (average size ~135 μm) spherical microcrystalline entities (the core) surrounded by a fine-grained matrix (average grain size ~1.5 μm) or a thick rim (the shell) distinguishable from the matrix. Tensile tests revealed yield strength of ~470 MPa that was accompanied by limited ductility (~2.8% plastic strain). Microstructure observation after testing showed debonding at interfaces between the matrix and the coarse entities, but in many instances, shallow dimples within the rim were observed indicating local ductile events in the shell. Dislocation emission and annihilation at grain boundaries and twinning at crack tip were the main deformation mechanisms taking place within the fine-grained matrix as revealed by in-situ transmission electron microscopy. Estimation of the stress from loop's curvature and dislocation pile-up indicates that dislocation emission from grain boundaries and grain boundary overcoming largely contributes to the flow stress.

1. Introduction

The mechanical behaviour and deformation mechanisms of nanocrystalline (NC) materials have been studied extensively for a few decades from both experimental and theoretical points of view. See for example refs [1–8]. In general, whatever the mode of processing, all of the studies, except for some special cases such as nano-twinned nickel [9–11], show that the performance obtained in terms of yield stress or strength is at the expense of tensile ductility, which consequently limits their formability. Therefore, different strategies have been proposed to improve the ductility of NC materials [12]. Among them, the implementation of bi- or multi-modal microstructures that incorporate more or less important volume fraction of coarse-grained (CG) particles into NC or ultrafine-grained (UFG) components has been suggested. To this end, powder metallurgy (PM) route is often used because of its versatility and successfully completed bimodal microstructures [13–17]. However, in such an intricate microstructure, it is often difficult to know exactly the contribution of each component on the overall mechanical behaviour. Also, the underlying deformation mechanisms of these components

* *Corresponding author*. Tel.: +33 1 49 40 34 88; fax: +33 1 49 40 39 38.
E-mail addresses: lfarban1@jhu.edu (L. Farbaniec), dirras@univ-paris13.fr (G. Dirras).
[1] Present address: Hopkins Extreme Materials Institute, Johns Hopkins University, 3400 North Charles Street, Baltimore, MD 21218, USA.

http://dx.doi.org/10.1016/j.matchar.2014.05.008
1044-5803/

cannot be investigated with the same tools. Intuitively, it can be claimed that the smaller grains will contribute to the strength increase, while the coarse grains to the ductility improvement. However, in a recent review, Estrin and Vinogradov [18] observed that bimodal microstructures processed by Equal Channel Angular Pressing do not lead to the ductility gain. The latter properties also depend on the processing route. For instance, bimodal microstructures processed from blends of nanometre-sized or UFG powder particles with CG ones may suffer grain boundary cracking [19] because of a residual porosity or contamination of powders, which therefore reduces the tensile ductility. Deformation incompatibility of different phases may also contribute to this effect. Nevertheless, PM techniques remain versatile routes for innovative microstructure design, and optimisation of these processes is required to better understand the deformation mechanisms that occur at different length scales or within the different constituents of the microstructure, and their potential interactions.

Nickel is a relatively abundant element found on the earth's crust that is used as the base in many alloy compositions intended for aeronautics, medicine or defense applications. In a pure form, e.g. electrodeposited, it has found an application in the field of micro-electro-mechanical-systems (MEMS) [20–22]. Other applications are liner for explosively formed projectile [23] and shielding for the containment of failed blades of auxiliary power units. These two applications have been motivated by its attractive mechanical properties, such as good ductility, high toughness and relatively low work-hardening rate. Cold worked to moderately high strength levels still maintain ductility. Therefore, the purpose of this study was to process and investigate mechanical properties of nickel samples with tailored microstructure that have enhanced strength and the desired ductility. To this end, electron backscatter diffraction (EBSD) and in-situ transmission electron microscopy (in-situ TEM) investigations were performed to analyse the deformation features occurring in multimodal nickel (M-Ni) processed by spark plasma sintering (SPS) of nanometre- and micrometre-sized powder particle blends. In the processed microstructure, special attention has been paid to the contribution of the fine-grained (FG) matrix component to the plastic deformation.

2. Experimental Procedures

2.1. Starting Powders

Two heterogeneous nanopowders (purity > 99.7%) having respectively a mean particle size of ~50 nm (ANi50) and ~100 nm (ANi100) were mixed with a coarse-grained (purity > 99.8%) powder aggregate (AANi) having particle size in the range of 100–150 μm. The ANi-type nanopowders were supplied by Argonide Corporation (Sanford, FL, USA) and fabricated by the so-called ELEX™ process [24], while Alfa Aesar (Ward Hill, MA, USA) supplied the AANi powder. Scanning electron microscopy (SEM) micrographs of the powders are presented in Fig. 1a–c. The blend was made of 200 g, 300 g, and 130 g of ANi50, ANi100 and AANi powders, respectively. The powder mixing was performed under protective atmosphere in a glove box and was homogenized using a Turbula™ mixer with helicoidally movement for 15 h. Following the mixing operation, the powder blend was cold pressed under a pressure of about 25 MPa in argon atmosphere to minimize powder oxidation before sintering.

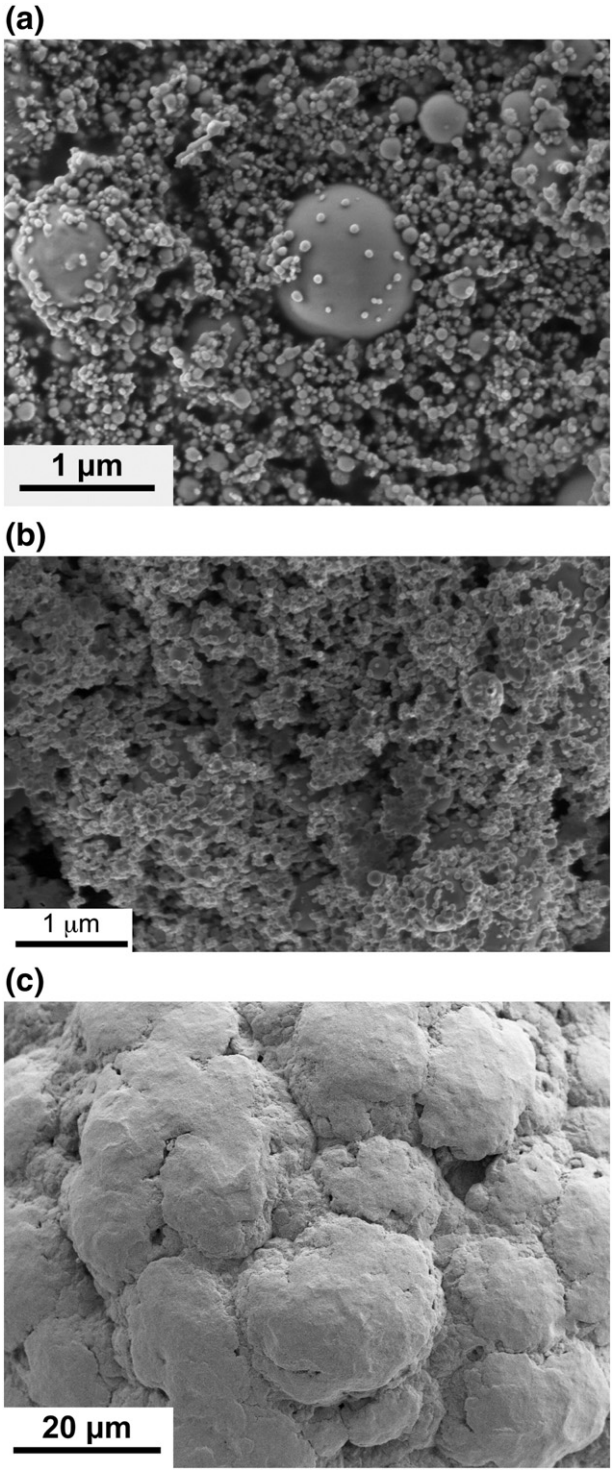

Fig. 1 – SEM images of the starting powders: (a) ANi50; (b) ANi100 and (c) AANi powders.

2.2. SPS Procedure

The sintering process was carried out in a SPS apparatus (HPD125 type) from FCT™ System GmbH due to the simultaneous application of direct current pulses of very high intensity (several thousands of amperes) and of a uniaxial pressure to the encapsulating system (Fig. A1 of Supplementary material 1). The powders were sintered for 30 min using a graphite die having an outer diameter of 90 mm and height of 50 mm. Actually, the powders were first cold compacted in the die lined with graphite foil at the sintering pressure for 5 min. Next, the die containing the cold-compacted sample was positioned between graphite punches with graphite foil between the compact powders and the punches. The die was then enveloped with a carbon felt to reduce the radiation heat losses from the outer surface. The SPS cycles were performed at a heating rate of 50 °C min^{-1} with a sintering temperature of 750 °C and an axial stress of 70 MPa, see Table 1. The temperature was monitored by K-type thermocouples located in a hole, which is about 3 mm away from the sample, RTC1, and at half height of the die in 80 mm deep hole, RTC4 and RTC6, and by a pyrometer positioned about 8 mm away from the sample (Fig. A2 of Supplementary material 1). Typical SPS output and the description of the cycles are provided in the Supplementary material (Fig. B1 of Supplementary material 1). Before the characterisation, the samples were polished using SiC 180 grit paper, next with diamond paste up to 1 μm, and finally cleaned in an ultrasonic ethanol bath to remove surface contamination from graphite foil. The relative density was obtained by the ratio of the bulk density of the sintered samples, determined using Archimedes method in distilled water, to the theoretical density. Each value is an average of three measurements (Table 1). Electro-thermal and thermo-mechanical simulations, performed with current and boundary temperatures at the spacers as input [25,26], revealed good temperature homogeneity of the SPS sample with the current tooling. Precisely, the temperature difference between the middle and the half-radius, and the middle and the exterior was found to be −1% and −2%, respectively. As a result of the process, discs of 30 mm in diameter were obtained, allowing the machining of tensile specimens (Fig. B2 of Supplementary material 1).

2.3. Tensile Tests

The tensile tests were performed at a constant displacement rate of 0.02 mm s^{-1}, providing a strain rate of 0.002 s^{-1} using a Testwell machine equipped with a load cell of capacity 50 kN. The strain was computed from the gauge length elongation. The latter was supplementary tracked by taking a photograph every 5 s of the marked initial gauge of 10 mm in length.

Table 1 – Specifications of the SPS cycles and measured relative densities for the two processed discs.

Sample	Sintering temperature (°C)	Axial stress (MPa)	Holding time (min)	Density (%)
MNi-1	750	70	15	97.8
MNi-2	750	70	15	98.4

2.4. Microstructure Investigations

2.4.1. EBSD Investigations

Following SPS process and tensile tests, the microstructures were examined using a Zeiss Supra 40VP Scanning Electron Microscope equipped with fully automated electron backscatter diffraction (EBSD) analysis system. The EBSD crystal orientation results were analysed with OIM™ Data Analysis software (version 4) from TexSem™ Laboratories. The orientation maps were obtained using a step size of 0.1 μm. For the EBSD examination, the specimens were ground using SiC grit papers up to SiC 4000 grade and finally polished in a colloidal silica solution (OP-S Struers) for 30 min.

2.4.2. In-Situ TEM Characterisations

In-situ TEM experiments were focussed on the contribution of the plastic deformation characteristics of the FG component of the processed microstructure. To this end, the specimens were prepared from the bulk material by cutting 3 mm × 1 mm × 0.5 mm rectangles, which were then mechanically ground. The obtained rectangles were either thinned down by electropolishing or by a combination of ion milling by the use of Precision Ion Polishing System (PIPS™, Gatan, Inc., Model 691) and a "flash polishing" using an A2 electropolishing solution from Struers at a voltage of 7 V for 5 s at room temperature. The latter preparation route was applied to circumvent the problem of the faster etching rate of the FG component compared to the CG one during electropolishing. Therefore, a fast electropolishing step, referred to as "flash polishing", was used to remove the damaged surface layer caused by ion milling [27]. The samples were then glued to a copper grid with cyanoacrylate that was eventually placed into a Gatan straining holder. The in-situ TEM experiments were carried out in a JEOL 2010HC microscope operated at 200 kV. Observations of the deformation mechanisms were recorded by a MEGAVIEW III camera at 25 fps in areas where the hole rim is parallel to the tensile axis, i.e. where the local stress is maximum [28].

3. Results and Discussion

3.1. Characteristics of As-Processed Microstructure

Fig. 2 shows typical microstructures of the as-processed M-Ni samples. It comprises CG multi-crystalline entities (the core) that are embedded in a FG matrix. In comparison with previous work where only ANi-type powders were used [19,29], the larger and highly subdivided CG entities (labelled CG1 in Fig. 2a–b) came from AANi powder, while the smaller and less subdivided ones (labelled CG2 in Fig. 2a–b) resulted from the two heterogeneous ANi-type powders.

Very often a thick shell (S) with variable thickness surrounding the spherical-like CG entities exists in the microstructure as it can be seen in Fig. 2a (see the shaded region) and Fig. 2d. Based on the SEM analysis, the size of CG core is about 135 ± 50 μm. These CG entities are subdivided into FG multi-crystals (average grain size of about 11.4 μm), whose grain size distribution is shown in Fig. 3a. The grain size distribution of the FG matrix follows a lognormal

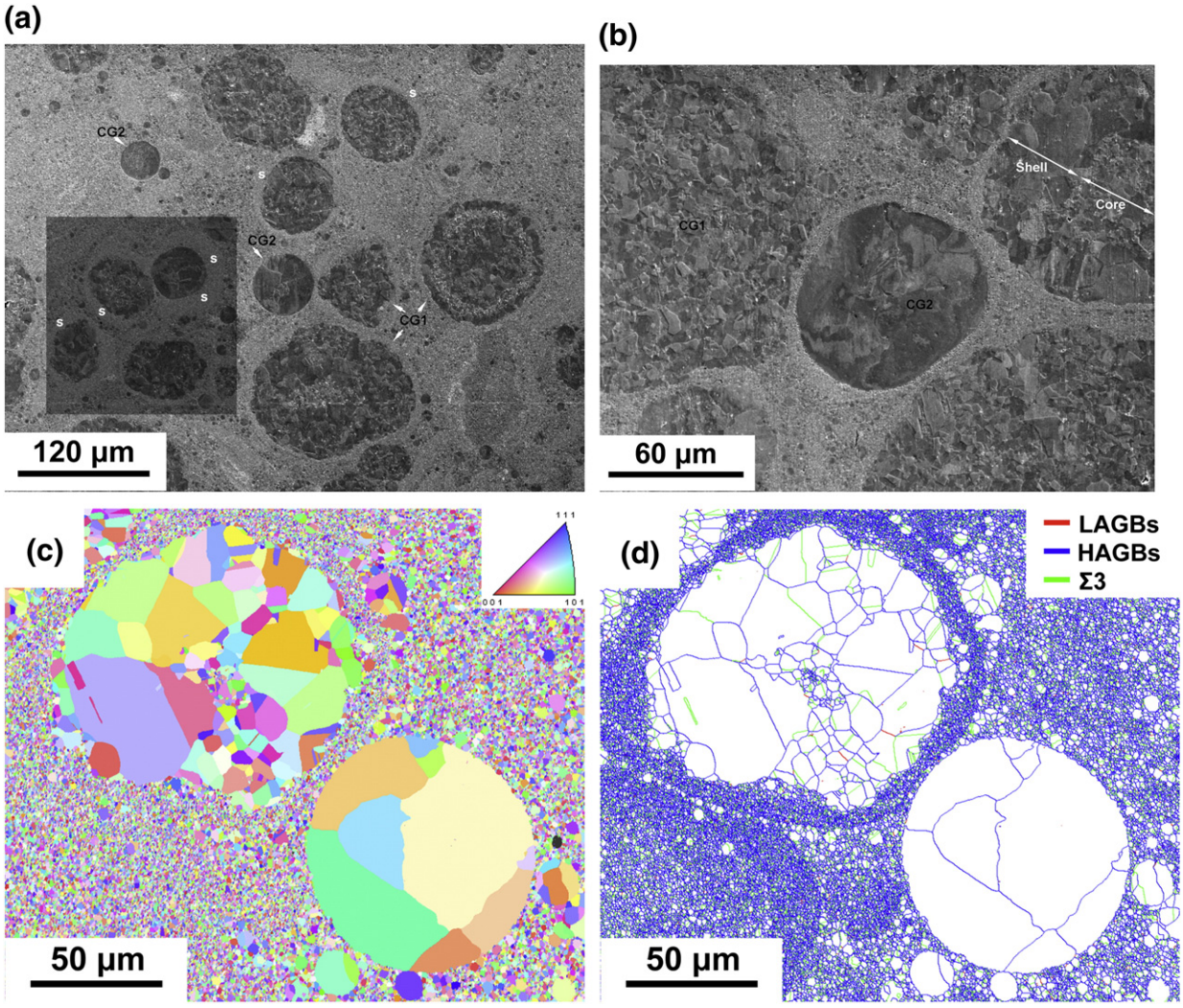

Fig. 2 – SEM micrographs (a, b) and EBSD maps (c, d) showing the different characteristics of the microstructure of as-processed M-Ni samples.

behaviour and is shown in Fig. 3b. The computed average grain size is about 1.4 μm, and is about one order of magnitude lower than that of the CG entities. As for the shell that occasionally surrounds the CG entities, the corresponding grain size distribution is presented in Fig. 3c. An average grain size of 5.3 μm was computed. Actually, from a local point of view, the grain size within the shell is variable in that it can be lower (as can be seen from Fig. 2a and d) or larger (as can be seen in Figs. 2b and 5a) than that of the FG matrix or the core (C) (Fig. 2b). These differences are not fully understood, and it is not clear at the moment why the shell forms and why it forms only around CG1-type powder particles. Most probably the difference in purity of the powders that were blended together plays a role during the SPS, as the current flow must be different because of a possible difference in the powder resistivity. It is interesting to note that when sintered separately using the same SPS processing parameters, none of the individual powders showed such features [29]. In addition, processing by hot isostatic pressing of a blend of ANi100 and a commercial purity CG Ni powder yielded bimodal microstructures without a shell surrounding the CG multi-crystalline entities [13]. Therefore it can be concluded that the observed features are due to the SPS specificity as described elsewhere [30]. Additional investigations are needed to clarify this point.

3.2. *Mechanical Properties and EBSD Analysis of the Deformed Samples*

Fig. 4 shows the true stress–true plastic strain curves after tensile test at room temperature at a strain rate of 0.002 s^{-1} for two samples with slightly different densities MNi-1 and MNi-2 (see Table 1). For comparison, the stress–strain curve of a CG nickel sample (Ni-CG) is also shown. After the onset of yielding, two regimes of hardening are observed. The first one occurs up to about 0.7% plastic deformation where the flow stress sharply increases from 470 MPa at yielding to about 550 MPa. The second and last regime occurs afterwards and corresponds to a limited flow stress increase of less than 20 MPa within a plastic deformation range of 0.7–2.8% (failure point).

Compared to the CG counterpart, there is an obvious increase of the yield stress as a consequence of a high fraction

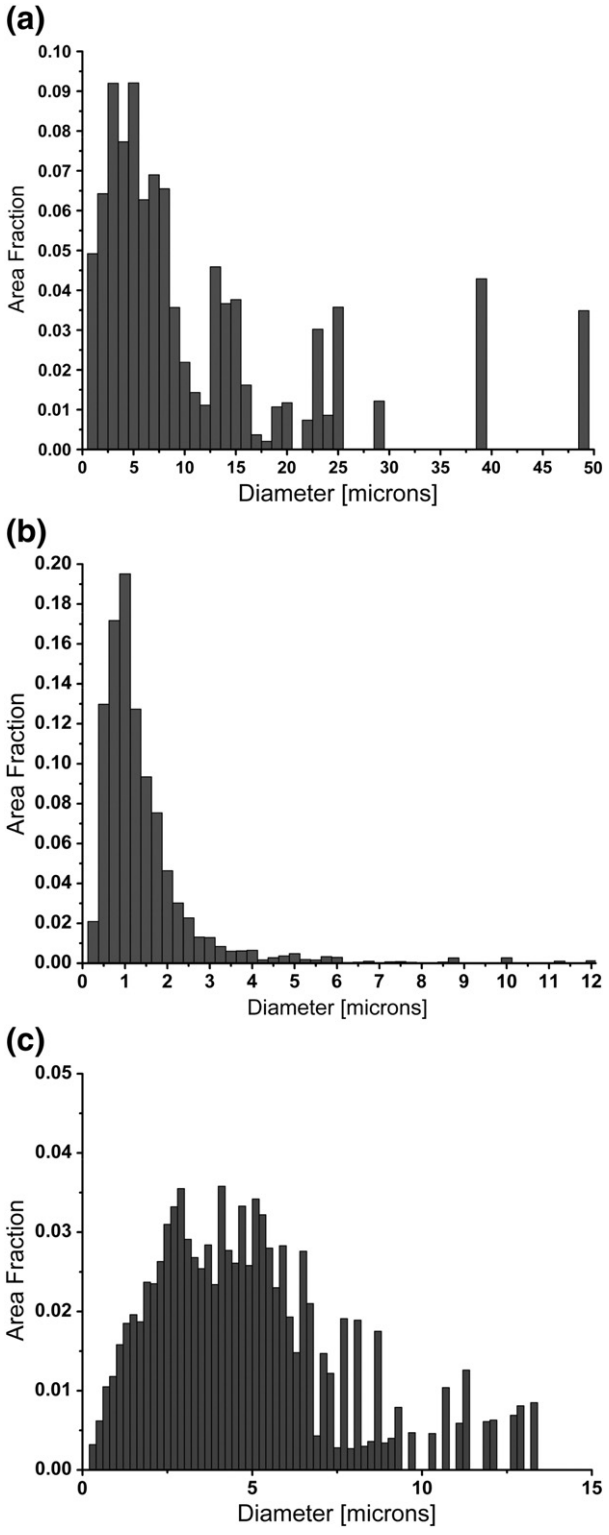

Fig. 3 – Grain size distributions of the different components of the microstructure extracted from EBSD experiments: (a) multi-crystallites inside CG entities; (b) FG matrix and (c) the shell surrounding some CG entities.

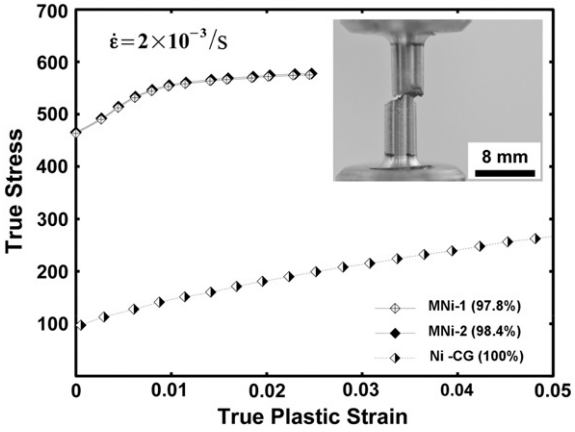

Fig. 4 – True stress–true plastic strain plots of room temperature tensile tests at 0.002 s^{-1}. Two samples from two consolidated discs were tested in the same conditions. The mechanical behaviour of conventional CG-Ni (average grain size of about 25 μm) is shown for comparison.

of the FG component as reported elsewhere [15,17,31,32]. In addition, contrariwise to a previous study on homogeneous UFG nickel processed via SPS and deformed in compression at room temperature [19], the softening behaviour that occurs just after the onset of yielding is not observed. Most probably, inter-granular micro-crack growth in the FG component and their subsequent propagation are delayed (or blunted) by the CG entities [17,31–33]. Further, crack network may build-up, which leads to stress saturation, and consequently to final failure as it is observed. This scenario is in good agreement with recent numerical studies performed on nanostructured metals with bimodal grain size distribution [34]. The contributions of micro-cracks in the plastic deformation were accounted for in the mechanism-based plastic model used to describe the strength and ductility of the bimodal metals. Indeed, it was shown that the cavitation micro-cracking controls the fracture mechanism in bimodal metals and alloys during tensile deformation, as usually observed in NC and FG materials. Recently, a novel microstructural design was proposed, the so-called "Harmonic Structure Design", which is a 3D network of FG shell with CG core, that results in a combination of high strength and high ductility at the same time [32,35,36]. Strain hardening rate analysis suggested that the early stage of deformation was dominated by the plastic deformation of the stronger FG shell region [36]. Therefore, at the early stages of deformation, it appears that the harmonic structure deforms in the same manner as the homogeneous FG microstructure, followed by typical deformation mode for CG materials in the later stages with a large uniform deformation. In this process, the CG component also undergoes plastic deformation to adjust the shape change of the FG shell in order to maintain the integrity of the material. However, in the present case, where a strong non-homogeneous grain size distribution exists, deformation incompatibilities may result in cracking and cavitation in the FG component, as observed by SEM and EBSD studies.

Fig. 5 shows SEM analysis of the fractured surface of the M-Ni sample after tensile tests. In Fig. 5a, large "dimples" homogeneously distributed in the sample cross-section can be seen. Enlarged view presented in Fig. 5b actually shows that they correspond to deformation features occurring due to

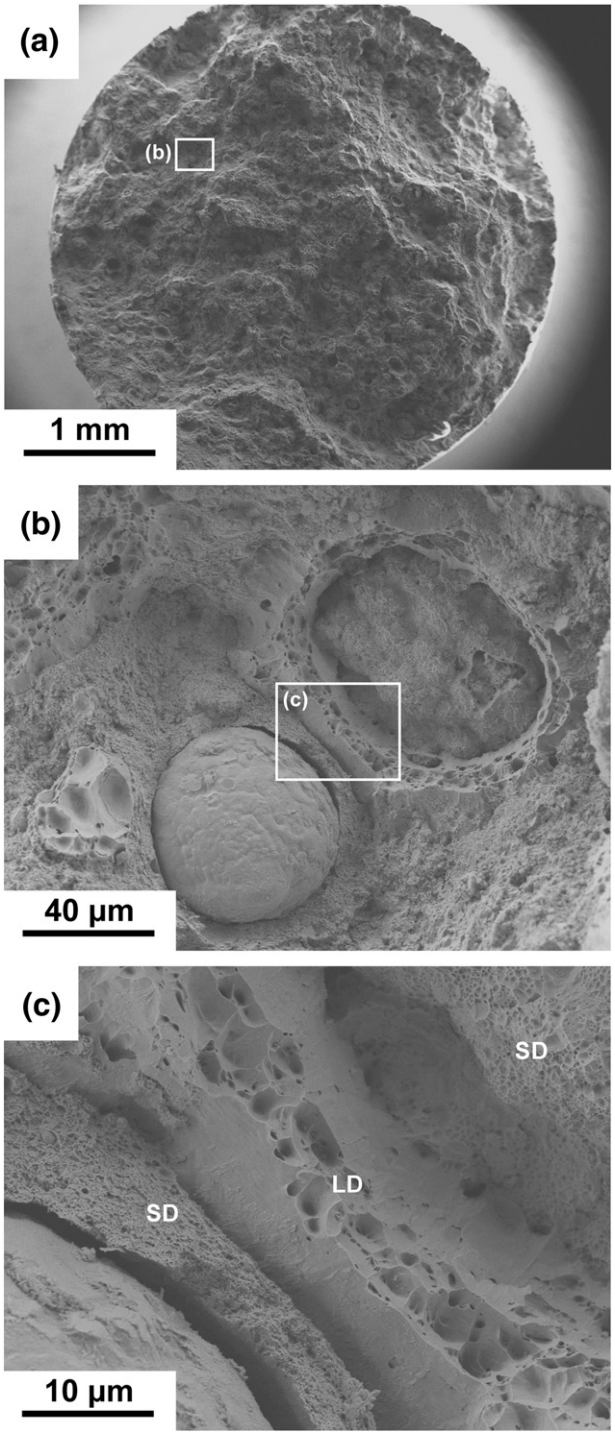

Fig. 5 – SEM images of fracture surface: (a) overall view; (b, c) enlarged view of a small area of (a).

the presence of the CG entities, which may be responsible for the overall tensile ductility. Still, the expected ductility was limited by a brittle-like failure and particle separation (debonding) from the matrix. A close view presented in Fig. 5c shows small dimples (marked SD) in the FG matrix adjacent to and beneath the CG entities (once they have been ejected). In addition, large and shallow dimples (LD) occur in what appear to be a periphery region or a shell around a CG entity accompanied by a shear-like fracture surface. It is therefore concluded that the shell plays an important role on the overall plastic deformation as it may induce further tensile ductility in the MNi samples compared to poor or zero tensile ductility observed in the bimodal case processed by our group so far [19,29]. It is possible that the debonding, as illustrated in Fig. 5c, comes from incomplete sintering. But, given the relatively higher mass density that was reached here, it is also possible that that grain size gradients influence the local behaviour, i.e. the larger the gradient the higher the probability of debonding or cracking due to deformation incompatibilities and stress concentrations as previously reported in [13,19]. Therefore, given the average grain size of the different components, the probability of debonding should be higher between the FG matrix and the CG entities than between the FG matrix and the shell. The presented results are in accordance with enhanced tensile ductility found in the case of the so-called "harmonic" structures made of CG core surrounded by UFG shell [37,38]. It is interesting to note that the ratio of the average grain size between the UFG shell and the CG core was the same as in the present study.

Further EBSD investigations confirm the above analysis. Fig. 6 shows EBSD maps of the specimen after failure (2.8% macroscopic plastic deformation), near the surface. In line with presented SEM observations, it was found that both the FG matrix and the periphery of the CG entities experienced a larger amount of plastic deformation than the centre (Fig. 6a–b). This is illustrated by the presence of low angle grain boundaries (LAGBs) in red colour (Fig. 6b). The amount of LAGBs is clearly higher within the periphery (the shell) and at the vicinity of cracking areas. The circular-like crack is probably due to a complex stress state that sets in the sample near the fractured surface. Interestingly it was observed that in the absence of a shell, the debonding phenomenon occurred all around the CG entity as shown in the inverse pole figure image (Fig. 6c).

3.3. *In-Situ TEM Investigations*

In-situ observations were carried out in areas of stress concentrations, i.e. close to crack tips. Because of residual porosities, cracks developed in regions of less resistance, more likely between voids. Fig. 7a shows the crack growth observed during straining experiments along a tensile axis oriented vertically on the images. As expected, the crack opened perpendicularly to the tensile direction and the crack path indicates that the fracture occurred preferentially along grain boundaries (GBs) of FG grains. However, observations of highly elongated grains, indicated by arrows in Fig. 7b, testified of significant plastic deformation. Dislocation activity has also been monitored inside the grain as shown below. NC grains, probably coming from the initial powder, are usually observed in the surroundings of FG grains and they may form small porosities, due to incomplete sintering as shown in Fig. 7c and d. This explains the reason why cracks preferentially propagated along these NC grains from porosities to porosities. These observations are also in agreement with reports of crack propagation in electrodeposited nickel along voids located at grain boundaries or triple junctions [39].

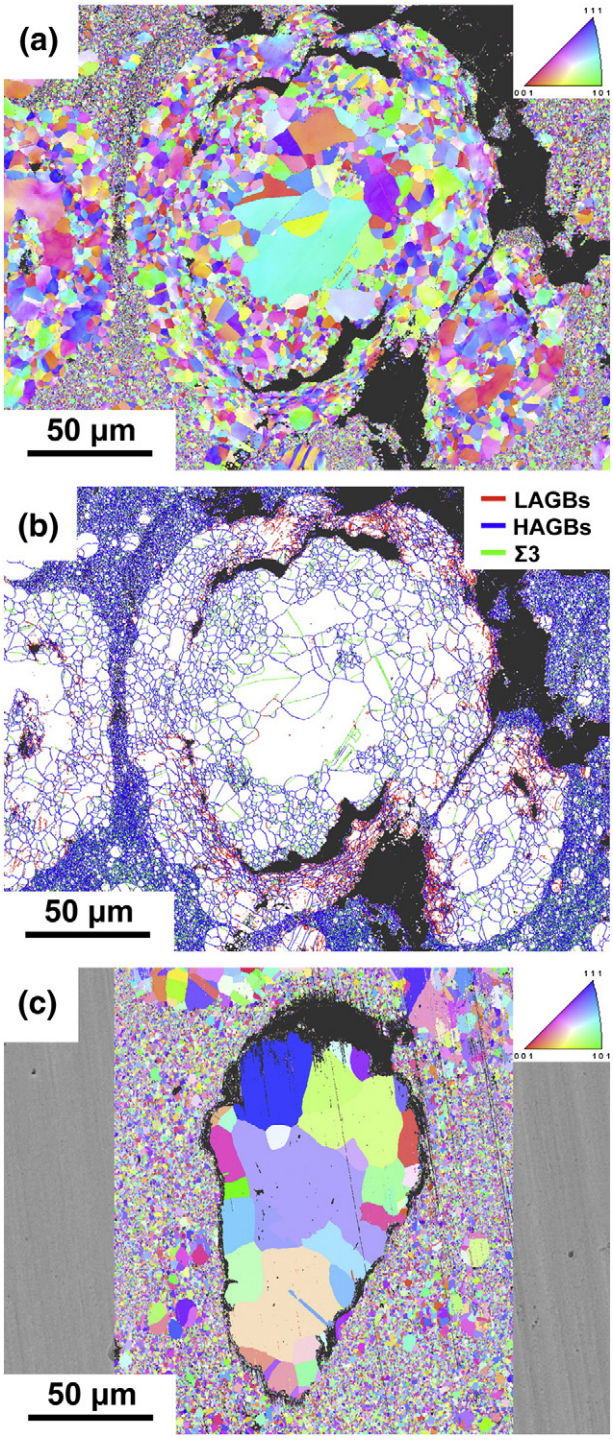

Fig. 6 – EBSD investigations near the fracture surface: (a–b) inverse pole image of a grain surrounded by a shell; (c) a grain without a shell.

Fig. 7d shows in more details an area containing NC grains close to GBs. It is worth noting that close to these NC grains, dislocation pinning (indicated by an arrow) can be observed evidencing the presence of very small obstacles, probably related to atomic impurities.

Fig. 8 and Video 1 (Supplementary material 2) illustrate plastic deformation in the grain, shown in Fig. 7c close to a crack tip (C). Under a tensile strain along the direction (T), dislocation emission arising from a source (S) has been observed. Although it is difficult to locate the source because of strong deformation close to GB; it appears to be close to a triple junction. At t = 0 s, a dislocation loop (d) is emitted in the grain interior and eventually expands rapidly (Fig. 8a–b). Fig. 8e represents schematically the process. One part of the dislocation intersects the sample surface and leaves a trace (tr) at one sample surface that can be identified as the (111) plane, as shown on the stereographic projection in Fig. 8c. The other part seems to be trapped close to the GB_2. The visibility of the dislocation with the [200] diffraction vector tends to indicate that the Burgers vector is either $\frac{1}{2}[1\bar{1}0]$ or $\frac{1}{2}[\bar{1}01]$. However, this latter yields an almost null Schmid factor. Because the glide plane normal is only 16° from the tensile direction, the dislocation is then expected to glide with a quite low Schmid factor M = 0.23 for a Burgers vector $\frac{1}{2}[1\bar{1}0]$. This can, however be explained since local high stress concentration at crack tip can arise.

Because mechanical tests tend to attribute the first stage of plastic deformation to the FG component, presumably in conjunction with crack development, the emission of dislocations from GB close to cracks followed by their piling-up is thought to be representative of the deformation mechanism in the early stage of plastic deformation. This conclusion needs however to be moderated by the fact that observations were carried in thin foils, which may introduce biases when compared to bulk materials. Usual surface effects on the dislocations such as image forces or surface pinning [40–42] can be neglected in the present case because the foil thickness is comparable to the distance between obstacles (i.e. the GBs). Crack propagation is however probably enhanced in thin foils because of the easy strain relaxation out of the thin foil plane. Long-range internal stresses that may exist in the bulk material are also lowered in thin foil conditions. Concerning more specifically GBs, diffusion processes such as dislocation climb may also be facilitated in a thin foil [43], which may affect the stress required to operate source and dislocation incorporation into GB. Dislocation nucleation in GB during in-situ straining experiments in UFG aluminium has been recently attributed to stress concentration at GB surface grooves [44].

The strength needed to activate the source can be estimated locally by measuring the dislocation curvature when the dislocation embryo just begins to expand. The shape of the dislocation in the (111) plane can be obtained by distorting Fig. 8a to correct the inclination of the glide plane with respect to the electron beam. Using anisotropic elastic calculations, the curvature of the dislocation can then be fitted by the theoretical equilibrium shape of a dislocation loop under a stress τ (through the DISDI software) [45].

The best fit (Fig. 8d) leads to $\tau = 110 \pm 10$ MPa, corresponding to an applied stress of $\sigma = \tau / M = 475 \pm 45$ MPa. This value, which is of the same order of magnitude as the measured macroscopic yield stress at 0.002 s^{-1}, i.e. σ_{YS} = 470 MPa, tends to indicate that the stress required to activate a dislocation source largely contributes to the overall yield stress.

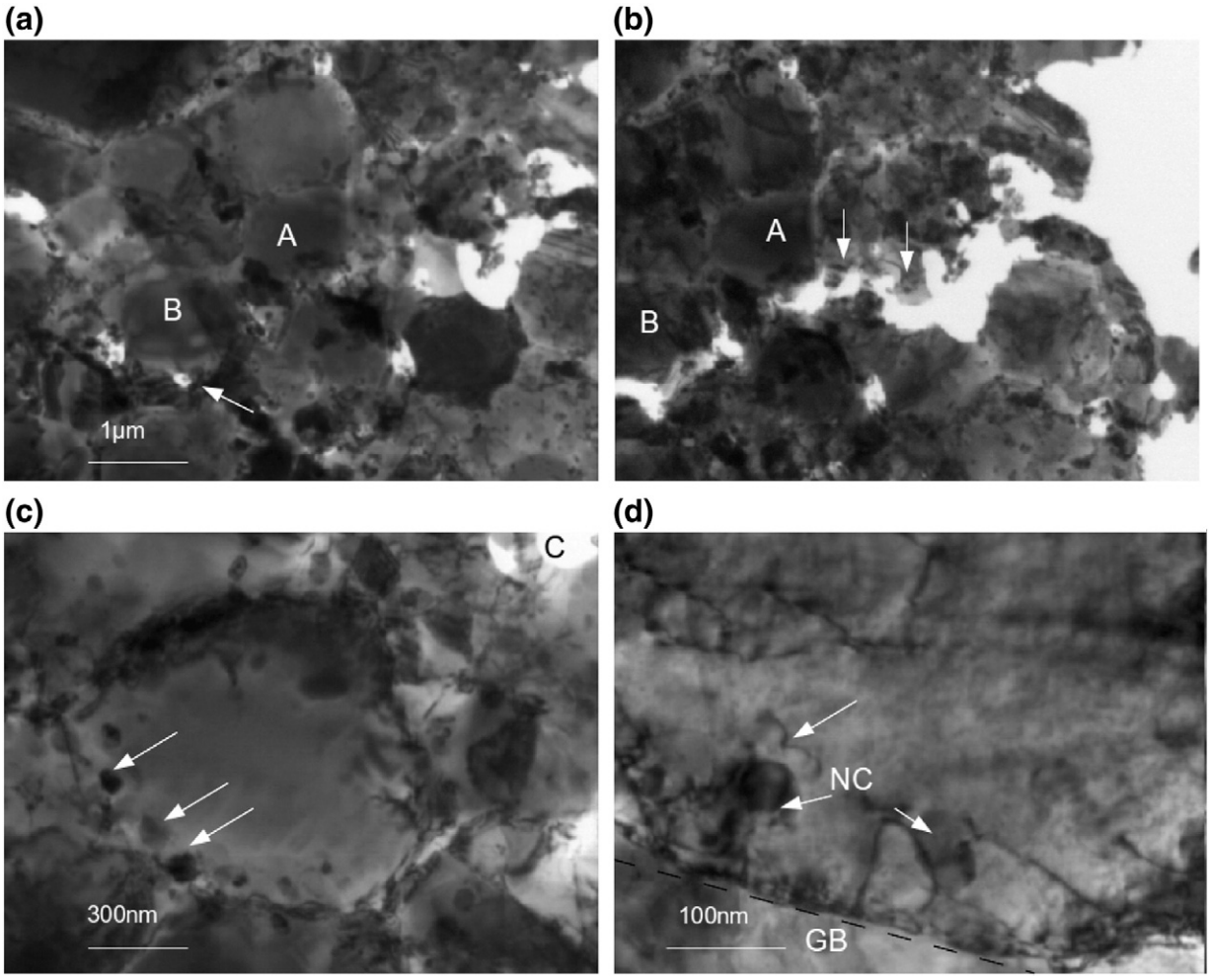

Fig. 7 – In-situ TEM observations in the FG matrix showing the influence of NC grains in deformation and damage mechanisms. See text for details.

Fig. 9a and Video 2 (Supplementary material 3) show that mechanical twinning is also possible in FG grains. A twin lamella (L) in a (111) plane and originating from a crack (C) (Fig. 9a) is clearly visible in grain G_1. It appears to be stopped at the GB between G_1 and G_2. Diffraction analysis shows that the GB is also a (111) twin, presumably an annealing twin. Upon straining, the twinning dislocations have been observed to move toward the GB (see the movie in the Supplementary materials). Although twinning is supposed to be disfavoured compared to perfect dislocation emission because of the formation of high stacking fault energy, it can occur in high stress concentration area where partial nucleation is easier [46] or in NC material due to the high line-tension energy of perfect dislocations [47]. Twinning has also been observed in NC nickel [48].

A closer inspection indicates that the lamella is in fact composed of two 20 nm thick twins (Tw), which are separated by a distance of about 30 nm (Fig. 9b). A zoom in the area of intersection between the twins shows that extrinsic dislocations have been emitted in the annealing twin, probably as the result of strain accommodation (Fig. 9c). As a matter of fact, no dislocation can be observed in the adjacent grain, but the disturbed diffraction contour ahead of the twin tip is an evidence of stress concentration in G_2 (Fig. 9d). It can be suspected that upon further straining, stress concentration in G_2 will lead to deformation transmission by emission of dislocations. The evaluation of the back stress that the annealing twin exerts on the twinning dislocation pile-up can be evaluated in first approximation by [49]: $\tau = (n\mu b / \pi l K)$, where $\mu = 76$ GPa is the shear modulus, $n = 81$ the number of dislocations, $b = 0.144$ nm the length of a twinning dislocation Burgers vector, $l = 1.3$ μm, the pile-up length and $K = 1 - v = 0.69$ for edge and $K = 1$ for screw dislocations. Although the Burgers vector of twinning dislocation has not been determined, the dislocation is thought to be $b = \frac{1}{6}[2\bar{1}1]$ corresponding to the dislocation with the highest Schmid factor (0.33) in the $(11\bar{1})$ plane [50]. In this condition, the dislocation has a pronounced screw character which leads to $\tau \sim 200$ MPa. This value is of the order of magnitude of the value measured above for dislocation emission. This indicates that annealing twins are strong obstacles to dislocation motion and thus promote strain hardening inside grains. Deformation propagation is then thought to occur by activation of sources from grain to grain, as observed above. The

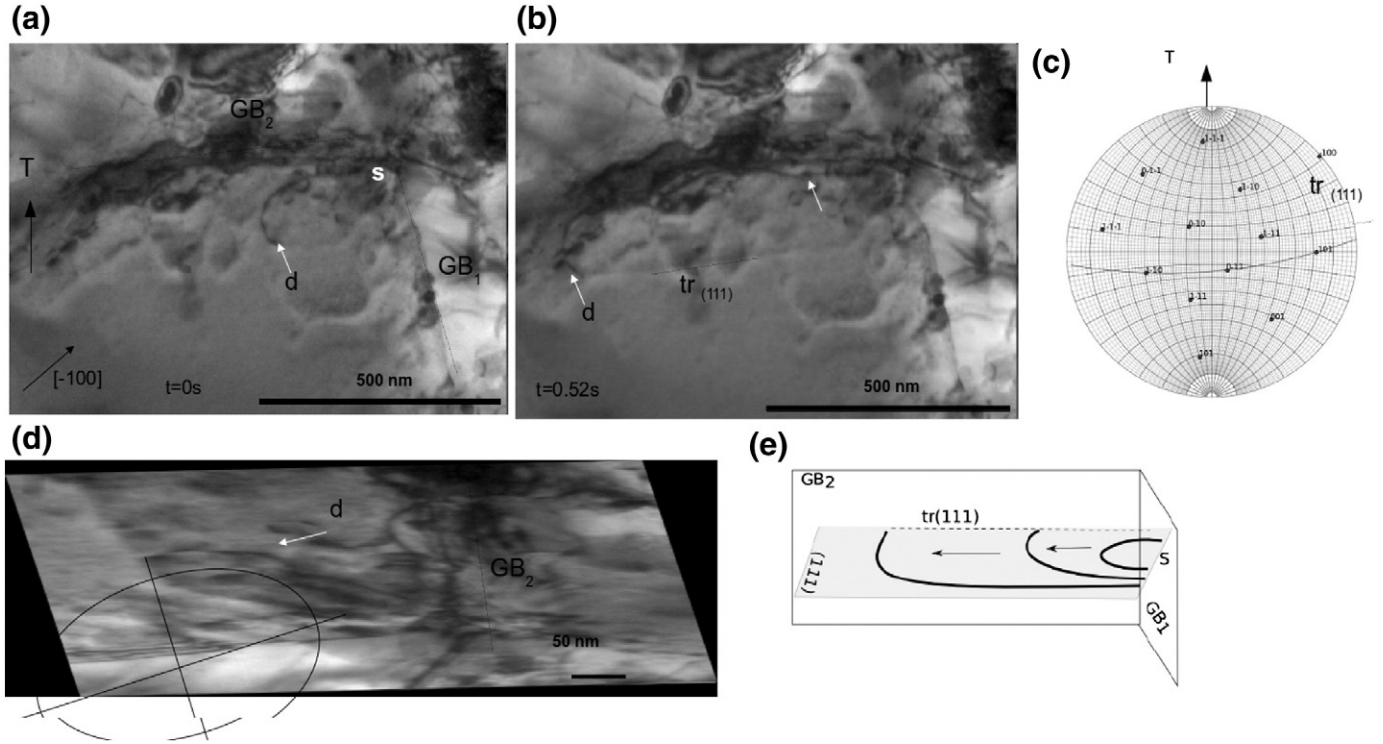

Fig. 8 – In-situ TEM investigation of plastic deformation in the grain shown in Fig. 7c close to a crack tip (see text for detail).

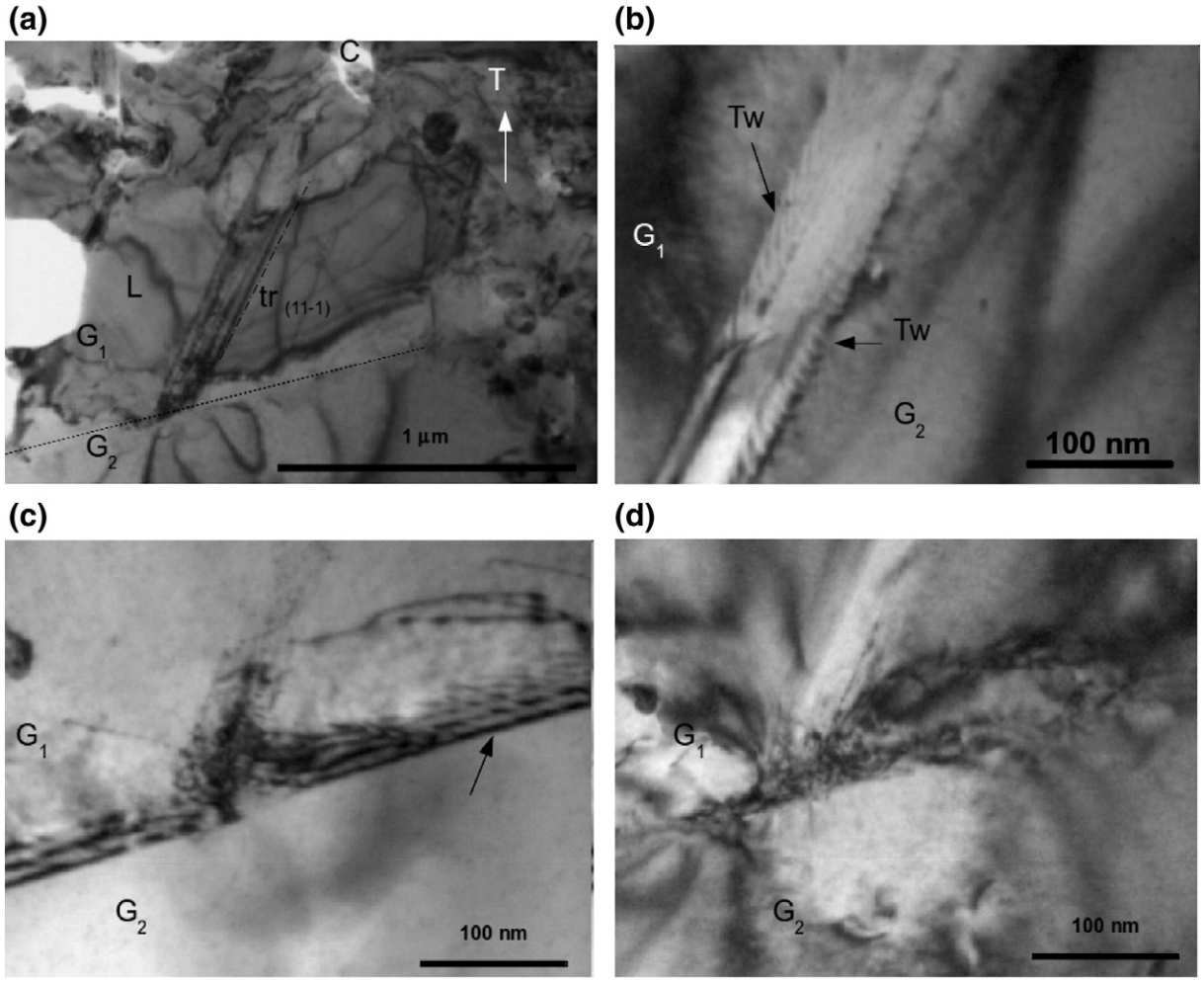

Fig. 9 – In-situ TEM image picturing twinning deformation mechanism within NC grains.

observation of dislocation motion in annealing twin is probably an efficient way to transfer strain and retard cracking. This process is also thought to be associated to very low thermal activation volume, i.e. high strain rate sensitivity [51]. These two characteristics of annealing twin, high strength and load transfer availability, are in line with observations of improved ductility and strength in nano-twinned copper [52].

Annealing twin boundaries are however special boundaries and the observations described above are only partly representative of deformation mechanisms occurring in the FG component. Most of the GBs are non-equilibrium HAGBs with a higher energy, and are thought to be "softer" compared to twin boundaries [53]. In such GB, deformation can however also be accommodated by incorporation and "delocalization" of intergranular dislocations, which is also a high strain rate sensitive mechanism [44,53].

4. Conclusions

SPS route was used to process multimodal bulk nickel samples from powder blends. Tensile tests showed mechanical strength enhancement (470 MPa) compared to conventional CG nickel but yielded moderate (macroscopic) plastic deformation of about 2.8%. Debonding at interfaces between the matrix and the coarse entities was observed probably as a consequence of large deformation incompatibilities due to a large difference in the grain size. Indeed, no crack and/or debonding were observed between the FG matrix and the FG rim as the average grain size was of the same order of magnitude. Therefore control of grain size gradient between the core and the shell appears to be of great importance for tensile ductility optimisation. Focussed on the FG matrix, in-situ TEM experiments showed that dislocation emission and annihilation at grain boundaries and twinning at crack tip were the main deformation mechanisms taking place within the FG component.

Supplementary data to this article can be found online at http://dx.doi.org/10.1016/j.matchar.2014.05.008.

Acknowledgements

This work was carried out in the framework of the "MIMIC" project funded by the French National Research Agency, ANR-09-BLAN-0010.

REFERENCES

[1] Kumar KS, Van Swygenhoven H, Suresh S. Mechanical behavior of nanocrystalline metals and alloys. Acta Mater 2003;51:5743–74.
[2] Meyers MA, Mishra A, Benson DJ. Mechanical properties of nanocrystalline materials. Prog Mater Sci 2006;51:427–556.
[3] Valiev RZ, Langdon TG. Principles of equal-channel angular pressing as a processing tool for grain refinement. Prog Mater Sci 2006;51:881–981.
[4] Saada G, Dirras G. The elastic–plastic transition in nanograined polycrystals. Int J Mater Res 2009;100:767–9.
[5] [Chapter 90]Saada G, Dirras G. Mechanical properties of nanograined metallic polycrystals. In: Hirth JP, Kubin L, editors. Dislocations in solids. Elsevier; 2009. p. 199–248.
[6] Wang YM, Ma E. Three strategies to achieve uniform tensile deformation in a nanostructured metal. Acta Mater 2004;52:1699–709.
[7] Van Swygenhoven H, Caro A, Farkas D. A molecular dynamics study of polycrystalline fcc metals at the nanoscale: grain boundary structure and its influence on plastic deformation. Mater Sci Eng A 2001;309–0:440–4.
[8] Schiøtz J. Atomic-scale modeling of plastic deformation of nanocrystalline copper. Scr Mater 2004;51:837–41.
[9] Jian WW, Cheng GM, Xu WZ, Yuan H, Tsai MH, Wang QD, et al. Ultrastrong Mg alloy via nano-spaced stacking faults. Mater Res Lett 2013;1:61–6.
[10] Lu L, Shen Y, Chen X, Qian L, Lu K. Ultrahigh strength and high electrical conductivity in copper. Science 2004;304:422–6.
[11] Dao M, Lu L, Asaro RJ, De Hosson JTM, Ma E. Toward a quantitative understanding of mechanical behavior of nanocrystalline metals. Acta Mater 2007;55:4041–65.
[12] Höppel HW, Zhou ZM, Mughrabi H, Valiev RZ. Microstructural study of the parameters governing coarsening and cyclic softening in fatigued ultrafine-grained copper. Phil Mag A 2002;82:1781–94.
[13] Dirras G, Gubicza J, Ramtani S, Bui QH, Szilágyi T. Microstructure and mechanical characteristics of bulk polycrystalline Ni consolidated from blends of powders with different particle size. Mater Sci Eng A 2010;527:1206–14.
[14] Dutel GD, Tingaud D, Langlois P, Dirras G. Nickel with multimodal grain size distribution achieved by SPS: microstructure and mechanical properties. J Mater Sci 2012;47:7926–31.
[15] Srinivasarao B, Oh-ishi K, Ohkubo T, Hono K. Bimodally grained high-strength Fe fabricated by mechanical alloying and spark plasma sintering. Acta Mater 2009;57:3277–86.
[16] Langlois P, Fagnon N, Dirras G. Microstructure engineering from metallic powder blends for enhanced mechanical properties. J Phys Conf Ser 2010;240:012016.
[17] Lee Z, Radmilovic V, Ahn B, Lavernia E, Nutt S. Tensile deformation and fracture mechanism of bulk bimodal ultrafine-grained Al–Mg alloy. Metall Mater Trans A 2010;41:795–801.
[18] Estrin Y, Vinogradov A. Extreme grain refinement by severe plastic deformation: a wealth of challenging science. Acta Mater 2013;61:782–817.
[19] Bui QH, Dirras G, Ramtani S, Gubicza J. On the strengthening behavior of ultrafine-grained nickel processed from nanopowders. Mater Sci Eng A 2010;527:3227–35.
[20] Hemker KJ, Last HR. Microsample tensile testing of LIGA Ni for MEMS applications. Mater Sci Eng A 2001;319–321:882–6.
[21] Buchheit TE, LaVan DA, Michael JR, Christenson TR, Leith SD. Microstructural and mechanical properties investigation of electrodeposited and annealed LIGA nickel structures. Metall Mater Trans A 2002;33A:539–54.
[22] Cho HS, Hemker KJ, Lian K, Goettert J, Dirras G. Measured mechanical properties of LIGA Ni structures. Sensors Actuators A Phys 2003;103:59–63.
[23] Couque H, Boulanger R. Explosively formed projectile simulations with Johnson–Cook models. In: Gálvez F, Sánchez-Gálvez V, editors. 23rd International Symposium on Ballistic, Tarragona, Spain; 2007. p. 255–62.
[24] Tepper F. Electro-explosion of wire produces nanosize metals. Met Powder Rep 1998;53:31–3.
[25] Wolff C, Mercier S, Couque H, Molinari A. Modeling of conventional hot compaction and Spark Plasma Sintering based on modified micromechanical models of porous materials. Mech Mater 2012;49:72–91.
[26] Wolff C. Modélisation du processus thermo-électro-mécanique de frittage flash. [PhD Thesis] Metz University; 2011.
[27] Veleva L, Schäublin R, Ramar A, Oksiuta Z, Baluc N. Focused Ion Beam application on the investigation of tungsten-based materials for fusion application. In: Richter S, Schwedt A, editors. EMC 2008 14th European Microscopy Congress 1–5 September, Aachen, Germany. Berlin Heidelberg: Springer; 2008. p. 503–4.
[28] Coujou A, Lours P, Roy NA, Caillard D, Clement N. Determination of the local tensile axis direction in a tem in situ strained γ' single crystal—a finite element approach. Acta Metall Mater 1990;38:825–37.
[29] Dutel GD. Comportement Mécanique et Mécanismes de Déformation et d'Endommagement de polycristaux de Nickel mono- et bi-modaux élaborés par SPS. [PhD Thesis], 13University of Paris; 2013.
[30] Orrù R, Licheri R, Locci AM, Cincotti A, Cao G. Consolidation/synthesis of materials by electric current activated/assisted sintering. Mater Sci Eng R Rep 2009;63:127–287.
[31] Billard S, Fondère JP, Bacroix B, Dirras GF. Macroscopic and microscopic aspects of the deformation and fracture mechanisms of ultrafine-grained aluminum processed by hot isostatic pressing. Acta Mater 2006;54:411–21.
[32] Zhang Z, Vajpai SK, Orlov D, Ameyama K. Improvement of mechanical properties in SUS304L steel through the control of bimodal microstructure characteristics. Mater Sci Eng A 2014;598:106–13.
[33] Dirras G, Tingaud D, Csiszár G, Gubicza J, Couque H, Mompiou F. Characterization of bulk bimodal polycrystalline nickel deformed by direct impact loadings. Mater Sci Eng A 2014;601:48–57.
[34] Zhu L, Shi S, Lu K, Lu J. A statistical model for predicting the mechanical properties of nanostructured metals with bimodal grain size distribution. Acta Mater 2012;60:5762–72.
[35] Orlov D, Fujiwara H, Ameyama K. Obtaining copper with harmonic structure for the optimal balance of structure–performance relationship. Mater Trans 2013;54:1549–53.
[36] Vajpai SJ, Ota M, Watanabe T, Maeda R, Sekiguchi T, Kusaka T, et al. The development of high performance Ti–6Al–4V alloy via a unique microstructural design with bimodal grain size distribution. Metall Mater Trans A 2014 [submitted for publication].
[37] Fujiwara H, Akada R, Noro A, Yoshita Y, Ameyama K. Enhanced mechanical properties of nano/meso hybrid structure materials produced by hot roll sintering process. Mater Trans 2008;29:90–6.
[38] Sekiguchi T, Ono K, Fujiwara H, Ameyama K. New microstructure design for commercially pure titanium with outstanding mechanical properties by mechanical milling and hot roll sintering. Mater Trans 2010;51:39–45.
[39] Douin J, Veyssière P, Beauchamp P. Dislocation line stability in Ni_3Al. Phil Mag A 1986;54:375–93.
[40] Couret A, Crestou J, Farenc S, Molenat G, Clement N, Coujou A, et al. In situ deformation in T.E.M.: recent developments. Microsc Microanal Microstruct 1993;4:153–70.

[41] Martin JL, Kubin LP. Discussion on the limitations of "in situ" deformation experiments in a high voltage electron microscope. Ultramicroscopy 1978;3:215–26.
[42] Legros M. In situ mechanical TEM: seeing and measuring under stress with electrons. C R Phys 2014;15:224–40.
[43] Wang Z, McCabe RJ, Ghoniem N, LeSar R, Misra A, Mitchell TE. Dislocation motion in thin Cu foils: comparison between computer simulations and experiment. Acta Mater 2004;52:1535–42.
[44] Mompiou F, Legros M, Boé A, Coulombier M, Raskin JP, Pardoen T. Inter- and intragranular plasticity mechanisms in ultrafine-grained Al thin films: an in situ TEM study. Acta Mater 2013;61:205–16.
[45] Wang Y, Chen M, Zhou F, Ma E. High tensile ductility in a nanostructured metal. Nature 2002;419:912–5.
[46] Zhu YT, Liao XZ, Wu XL. Deformation twinning in nanocrystalline materials. Prog Mater Sci 2012;57:1–62.
[47] Zhang XY, Wu XL, Zhu AW. Growth of deformation twins in room-temperature rolled nanocrystalline nickel. Appl Phys Lett 2009;94:121907.
[48] Hirth JP, Lothe J. Theory of Dislocations. New York: John Wiley & Sons; 1982.
[49] Lu L, Schwaiger R, Shan ZW, Dao M, Lu K, Suresh S. Nano-sized twins induce high rate sensitivity of flow stress in pure copper. Acta Mater 2005;53:2169–79.
[50] Christian J, Mahajan S. Deformation twinning. Prog Mater Sci 1995;39:1–157.
[51] Lu L, Chen X, Huang X, Lu K. Revealing the maximum strength in nanotwinned copper. Science 2009;323:607–10.
[52] Priester L. Grain boundaries and crystalline plasticity. Wiley, John & Sons; 2011.
[53] Mompiou F, Caillard D, Legros M, Mughrabi H. In situ TEM observations of reverse dislocation motion upon unloading in tensile-deformed UFG aluminium. Acta Mater 2012;60:3402–14.